Grain size and texture dependence on mechanical properties, asymmetric behavior and low temperature superplasticity of ZK60 Mg alloy

Ehsan Mostaed [a,*], Alberto Fabrizi [b], David Dellasega [c], Franco Bonollo [b], Maurizio Vedani [a]

[a] Department of Mechanical Engineering, Politecnico di Milano, Milan, Italy
[b] Department of Management and Engineering, Università di Padova, Stradella S. Nicola 3, 36100 Vicenza, Italy
[c] Department of Energy, Politecnico di Milano, Milan, Italy

Received 20 December 2014
Received in revised form 6 May 2015
Accepted 15 June 2015
Available online 2 July 2015

1. Introduction

Due to the low density, high specific strength and stiffness, excellent damping capacity and biocompatibility, magnesium and its alloys have been attracting much attention as potential metallic materials in a wide range of automotive, military, electronic, aerospace and biomedical ap-plications [1–6]. However, Mg exhibits poor formability at room tem-perature due to its hexagonal closed-packed (HCP) crystal structure with limited number of available slip systems. Plastic deformation of Mg and its alloys is mainly dominated by basal slip {0 0 0 1} <1120> since critical resolved shear stress (CRSS) of the basal slip system is far below those of the non-basal slips of <a> type dislocations on prismatic {1010} and pyramidal {1011} planes [7]. Basal plane alone provides only two independent slip systems which are much fewer than those re-quired, five independent slip systems, to fulfill the Taylor criterion [8], leading to poor formability of Mg at room temperature. However, with increasing of temperature, the CRSS of non-basal slip systems decreases gradually, while that of basal slip remains constant. Accordingly, non-basal slip mechanisms are responsible for improved formability of Mg at elevated temperatures (>180 °C) [9,10]. Since the non-basal slip mechanisms are only observed at high temperatures, plastic deformation in polycrystalline Mg alloys appears to be governed entirely by basal slip system at room temperature [11]. Furthermore, insufficient active slip systems in such a crystal structure results in the formation of a strong crystallographic texture upon thermo-mechanical processes. Therefore, conventionally extruded and rolled Mg alloys show a strong basal texture at which the basal planes are predominantly aligned par-allel to the main plastic flow direction, inducing poor deformability and strong anisotropy [12,13]. In general, Mg is a low-symmetry material due to activation of the {1 0 1 2} <1011> extension twin, when tensile and compression stresses are perpendicular and parallel to the basal planes, respectively, producing marked tension–compression yield asymmetry. Hence, structural applications in which samples are simul-taneously subjected to tension and compression loading are limited. Therefore, minimizing the asymmetry effect is of major importance for a widespread commercial acceptability. Previous studies have demonstrated that this mechanical anisotropy can be modified by several ways such as texture weakening [14,15], grain refinement [14–16], association of alloying elements [17] and heat treatment [18]. Among the mentioned approaches and factors, texture and grain size make sig-nificant contributions to the mechanical asymmetry, though the indi-vidual influences of the grain size and texture on yield asymmetry and also the dominant factor when they are combined, have yet to be clarified.

* Corresponding author.
E-mail address: Ehsan.mostaed@polimi.it (E. Mostaed).

It is well known that grain refinement, especially in ultra-fine regime obtained by severe plastic deformation (SPD) methods, leads to im-proved mechanical properties and remarkably enhanced superplasticity through grain boundary-sliding (GBS) [15,16,19,20]. It is also proved that GBS contribution to the total plastic flow increases with decreasing the grain size. The materials processed by SPD methods exhibit super-plasticity at even low temperatures ($<0.5T_m$ where T_m is the absolute melting temperature) [21,22]. However, also for this straining condi-tion, the texture and grain size dependence on superplastic ductility and plastic flow is still not obvious. In the present study attempts have been made to comprehensively investigate the effects of texture and grain size, both separately and simultaneously on mechanical, asym-metric behavior, superplasticity and deformation mechanism of a ZK60 Mg alloy.

2. Experimental procedure

2.1. Materials and methods

A commercially available extruded ZK60 (Mg–5.3Zn–0.48Zr, wt.%) alloy was selected for this study. Equal channel angular pressing (ECAP) was conducted using a die with an intersecting angle and outer arc of curvature of 110° and 20°, respectively. According to the Iwahashi formula [23], this geometry creates an equivalent shear strain of 0.76 on each pass. To successfully refine the grain structure, ECAP was carried out according to a three-step strategy with decreasing temperature levels of 250 °C, 200 °C and 150 °C. For each level four ECAP passes were used. In order to eliminate the ultra-fine grained (UFG) effect as a probable origin of extraordinary mechanical behavior, and in addition, to study the effect of the texture separately, a set of UFG samples was annealed at 350 °C for 2 h. Table 1 summarizes the conditions investigated for the ZK60 alloy at different ECAP temperatures. All the samples were subjected to repetitive pressings with a 90° clockwise rotation of the billet between the successive passes, according to the procedure designated as route B_C in the literature [24].

2.2. Microstructural and texture characterization

All the samples were microstructurally characterized by the Electron Backscatter Diffraction (EBSD) technique on the longitudinal plane. Grain size distribution, crystallographic texture and grain orientation maps of ZK60 alloy in the as-received condition and after the ECAP process were obtained using the EBSD technique interfaced with a field emission gun scanning electron microscope (FEG-SEM). All the data were then processed with TSL OIM™ software. The typ-ical scan area was 30 μm × 30 μm with a 0.12 μm step size for the ECAP-processed specimens while, in the case of the samples with coarser grains (e.g., A and E3A), a larger area was scanned to cover adequate number of large grains for a reliable statistical analysis. Prior to the EBSD analysis, all specimens' surfaces were carefully pre-pared by standard mechanical polishing followed by a low-angle ion milling.

Table 1
ECAP processing conditions of the investigated samples.

Sample code	Treatment history
A	As-extruded ZK60 Mg alloy
E1	ECAP treatment for 4 passes at 250 °C
E2	E1 + further ECAP treatment for 4 passes at 200 °C
E3	E2 + further ECAP treatment for 4 passes at 150 °C
E3A	E3 + annealing treatment at 350 °C for 2 h

2.3. Mechanical characterization

Mechanical properties were characterized by tensile and compression tests. Tensile specimens with a gage length of 12 mm and a diameter of 4 mm were machined along the longitudinal direction of the specimens and tested at room temperature at an initial strain rate of $1.0 \times 10^{-3}\ s^{-1}$, while characterization of the superplastic behavior was carried out at 200 °C with strain rates ranging from $1.0 \times 10^{-4}\ s^{-1}$ to $1.0 \times 10^{-1}\ s^{-1}$. Compression tests were performed at room temperature at a strain rate of $1.0 \times 10^{-3}\ s^{-1}$ on cylindrical specimens with a diameter of 10 mm and height of 20 mm, cut along the processing direction from the as-extruded and ECAP processed billets. Standard deviations were calculated in each case out of a popu-lation of three experiments.

3. Results and discussion

3.1. Microstructural and texture characterization

Fig. 1 shows the microstructural evolution and corresponding grain size distribution of samples during the ECAP process. As seen in Fig. 1a, the starting sample possessed a rather bimodal structure with coarse grains of about 20 μm and fine grains of about 1–3 μm giving a mean grain size of 5 μm. Moreover, the distribution of the grain bound-ary misorientations shows a relatively high fraction of high-angle grain boundaries (HAGB) of ~76%, confirming the occurrence of DRX during extrusion. With ECAP process advancement, clear grain refinement oc-curred. However, some coarse grains representing the residual part of the original structure remained (Fig. 1b and c). Finally, at the last step of ECAP (sample E3) those large grains were also refined and an almost uniform and equiaxed ultra-fine grain (UFG) structure was obtained with a mean grain size of 500 nm (Fig. 1d). Fig. 2 shows the SEM images of E3 and E3A, taken in a back-scattered electron (BSE) mode at two dif-ferent magnifications. Fig. 2a and c shows reasonably uniform dispersed small particles mainly in the range of less than 100 nm (see the inset on the top corner of Fig. 2c). After annealing at 350 °C for 2 h, as seen in Fig. 1e, not only a considerable grain growth occurred, but also precipi-tation coarsening was observed (Fig. 2b and d). In other words, the very fine second phase particles induced by ECAP coalesced into larger ones with size of tens of times bigger due to the annealing treatment, minimizing the effect of precipitation hardening. The coalescence of the pre-cipitates along with grain growth in E3A sample might cause a significant reduction in mechanical strength which will be discussed in the next section. The (0002) pole figures of the investigated samples are shown in Fig. 3. As seen in Fig. 3a, sample A exhibited a very pronounced <1010> fiber texture in the initial condition, as the typical ex-trusion texture by which basal planes are parallel to the extrusion direction. However, this dominant texture gradually attenuated during ECAP processing and was eventually replaced by a new strong texture with basal planes preferentially inclined to the ECAP direction in sample E3 (Fig. 3a to d). It is worth mentioning that the maximum texture in-tensity consistently increased with ECAP progress from 7.5 up to 20.2 for A and E3, respectively. Such a strong texture obtained through the ECAP proc-ess is attributed to the use of route B_C representing a highly redundant strain path [25]. Table 2 summarizes the average Schmid factor values of (0 0 0 1) <11$\bar{2}$0> basal slip and {1 0 $\bar{1}$ 2} <10$\bar{1}$1> extension twin for all the investigated samples. It can be seen that with increasing number of ECAP passes significant improvement of Schmid factor value of basal slip from 0.16 to 0.34 for A and E3 samples, respectively, was achieved. The increase in Schmid factor value results in easy dislocation slip on the dominant slip plane (0 0 0 2) and thereby, lowers the stress required for yielding, improving the ductility at room temperature. In brief, it can be observed that continuous increase in texture intensity from 7.5 to 20.2 and in the basal slip Schmid factor from 0.16 to 0.34 during the ECAP process, gave rise, respectively, to the formation of a

much stronger texture and a more favorable condition for dislocation slip, in sample E3. Considering A and E3 samples, having two different grain sizes and different texture orientations, the effect of grain size and texture on mechanical properties cannot be distinguished. After annealing (E3A), as seen in Fig. 1e, although the UFG structure was replaced by a micrometer-size grain structure which is comparable with that of sample A, the basal texture orientation was only slightly modified from the previous condition (E3; basal planes coincident with the

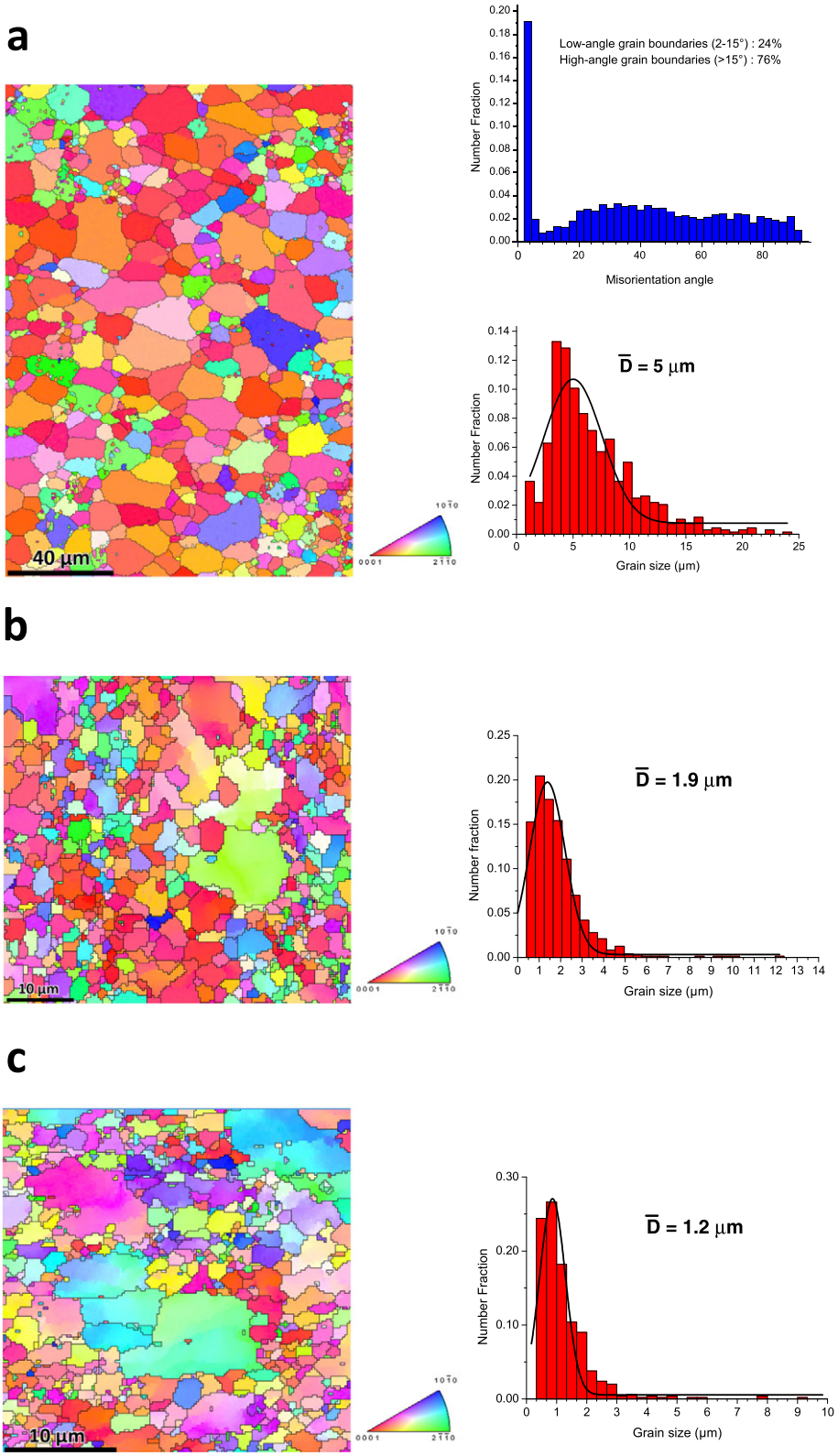

Fig. 1. EBSD orientation map and corresponding grain size distribution of (a) A, (b) E1, (c) E2, (d) E3 and (e) E3A samples.

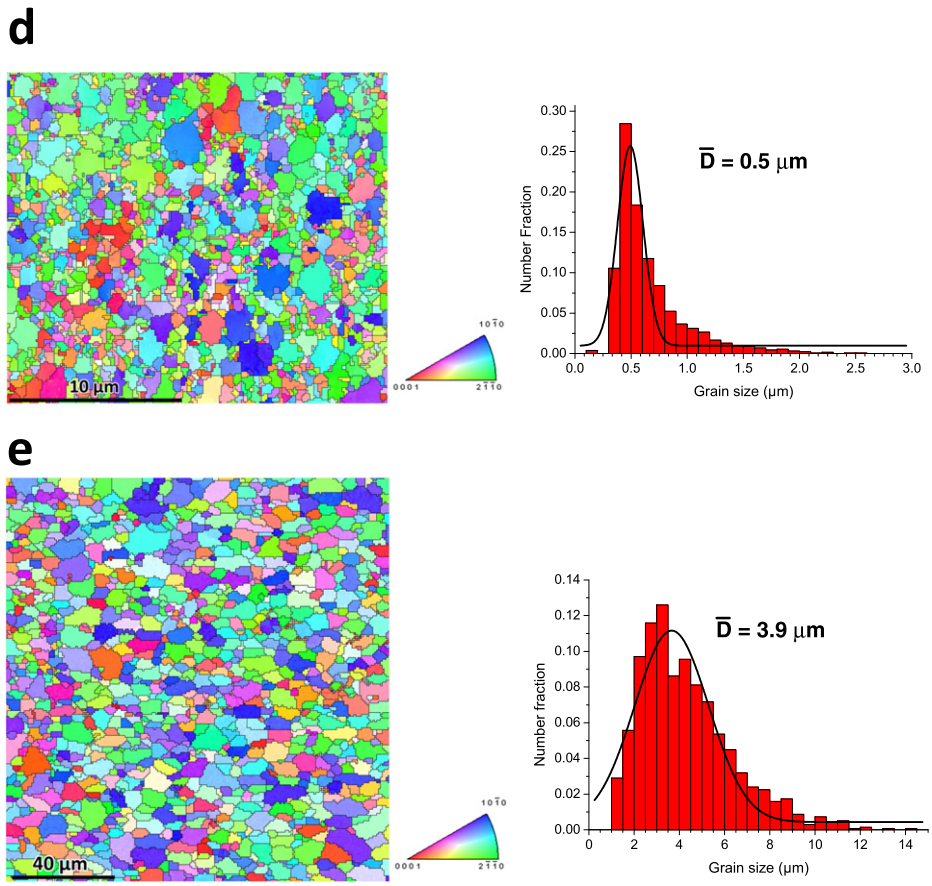

Fig. 1 (*continued*).

ECAP shear plane) with a moderate decrease in the maximum texture intensity down to 15.5 (Fig. 3e). Accordingly, texture and grain size effects could be separately investigated by pairwise comparison of A, E3 and E3A conditions (A and E3A have close grain size but different textures, E3 and E3A have the same texture orientation but different grain sizes).

3.2. Mechanical properties at room temperature

Fig. 4a shows the yielding asymmetry ratio (AR) represented by the ratio of the tensile to compression yield stress. In the starting condition, a considerably high AR value of 1.8 was calculated which is due to a strong extrusion texture with the majority of the basal planes lying par-allel to the extrusion direction, resulting in generation of $\{\bar{1}0\ 1\ 2\}\langle 10\bar{1}\ 1\rangle$ twins. It is well established that, extension twining becomes activat-ed when the compression load axis is parallel to the basal planes [13]. As seen in Table 2, the obtained Schmid factor values for basal slip and ex-tension twining are 0.16 and 0.42, respectively, indicating the high like-lihood of activation of extension twining since the stress needed to activate twinning is less than that needed to activate basal slip, leading to large AR value. However, this ratio significantly decreased even after the first ECAP step to 1.2, which is attributed to the higher increasing rate of twinning stress than that of slip due to the degradation of twin-ing Schmid factor value by ECAP progress (see Table 2) as well as grain refinement, making twinning less favorable and eventually leading to similar tensile and compression yield strength behavior [26]. Further ECAP passes led to AR of 0.9 and 1.1 for E2 and E3, respectively. In the case of E3A with an almost similar basal texture to E3, in spite of the remarkable grain growth, almost no yielding asymmetry was observed ($AR = 0.92$). Furthermore, compared to sample A, the lower Schmid factor value for {1 0 1 2} twinning of E3A sample makes the activation of extension twining more difficult, resulting in almost no yielding asymmetric behavior observation. Thus, it can be concluded that yield asymmetry is strongly influenced by basal plane orientation rather than grain size.

All the main tensile parameters including the tensile yield stress (TYS), ultimate tensile strength (UTS) and fracture elongation (FE) are presented in Fig. 4b. Considering the clear grain refinement from A to E2 condition, it is suggested that both TYS and UTS decreased owing to significant increment of texture intensity and Schmid factor, making plastic deformation easier, as discussed above. In other words, the tex-ture development is the dominant factor in the first two ECAP steps, overwhelming the grain refinement strengthening effect and leading to a net decrease in both TYS and UTS from 290 and 339 MPa to 216 and 308 MPa, respectively, along with an improved fracture elongation. Further grain refinement, namely when moving from E2 to E3 samples, leads to considerable improvement in both strength and fracture elon-gation up to 273 MPa and 30%, respectively, which represents a compro-mise between grain refinement effect and favorable basal plane sliding and GBS. That is, increased in tensile strength is associated with grain boundary and precipitation strengthening which are arisen from UFG structure (Fig. 1d) and homogenous distribution of the very fine second phase particles (Fig. 2c), respectively, while higher basal slip Schmid factor and GBS which can be activated even at room temperature in UFG structures [27] are responsible for softening. It is supposed that these two latter effects would improve fracture elongation as well. After annealing (E3A), the TYS dramatically dropped from 273 to 122 MPa. Given the difference with E3 condition, it can be supposed that grain and precipitate coarsening (suppression of grain boundary and precipitation strengthening, respectively) along with the high value of Schmid factor for basal slip (0.38, see Table 2), leading to a de-creased yield stress in E3A sample. Indeed, the observed TYS value for

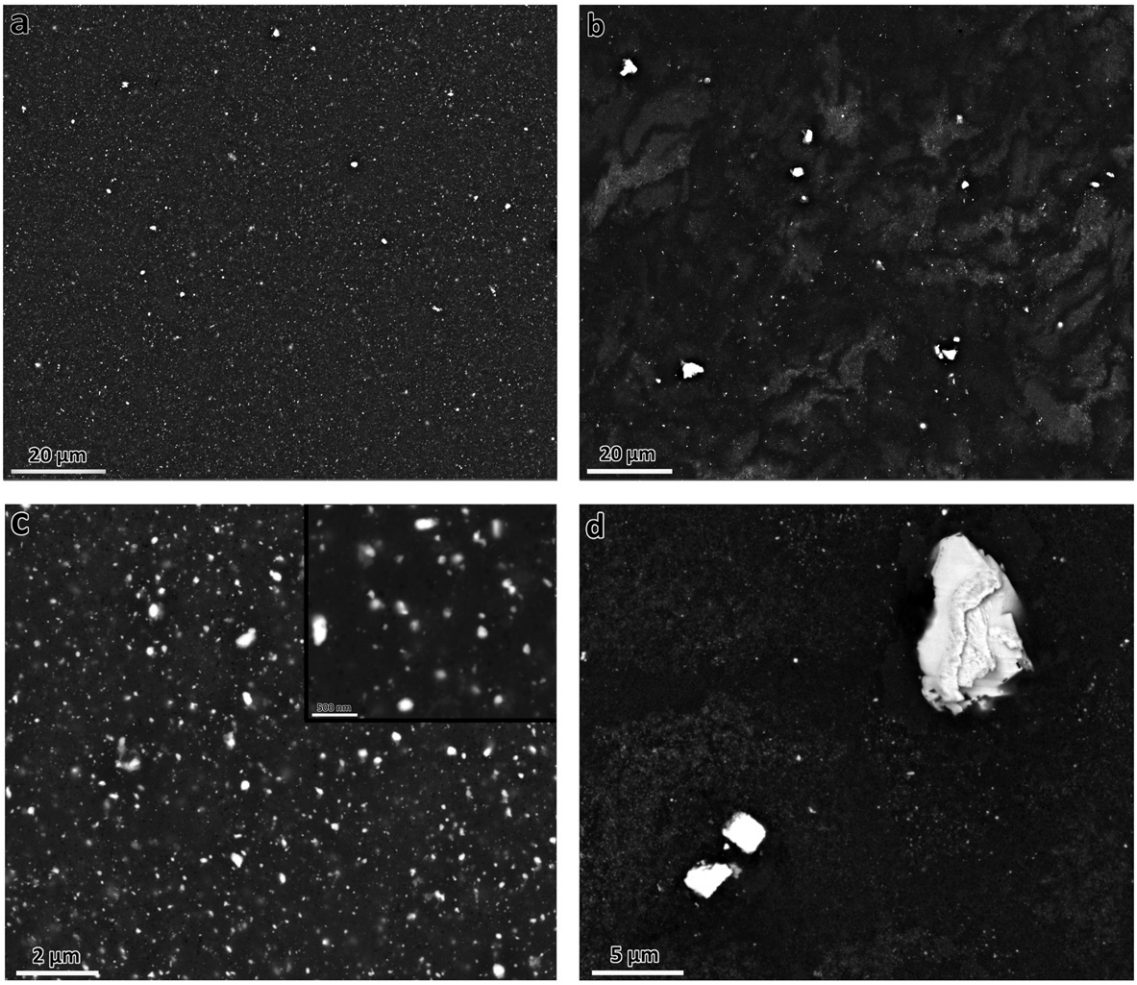

Fig. 2. Back-scattered electron SEM images of E3 (a and c) and E3A (b and d).

E3A samples is even far below (less than half) that of A condition although both possess a close grain size. Therefore, the Hall–Petch effect alone is obviously inadequate for explaining the extent of the TYS drop. Inevitably, it is concluded that the difference in measured TYS values is also strongly influenced by the two different basal texture orientations in the two samples. As a further evidence, E3A exhibited a meaningful increase of the uniform elongation up to 43% which is about three times as high as that of the extruded alloy (A). Fig. 4c depicts a strong decrease in work hardening exponent (from 0.15 to 0.05) with ECAP progress from A to E3. This behavior confirms the con-tribution of GBS to the deformation [28]. After annealing, due to the high activity of basal slip, the work hardening exponent considerably in-creased to 0.3. It should be noted that decreases in volume fraction of precipitates and dislocations, due to the annealing treatment are re-sponsible for such a high strain hardening exponent measured for sam-ple E3A. Combination of low yield stress and good hardening response provides a potential for a very extensive formability for E3A condition, featuring a high UTS value of 273 MPa.

Fig. 5 depicts SEM fractographs of A, E3 and E3A samples tested at room temperature. As seen in Fig. 5a, on the fracture surface of A large fraction of cleavage planes and dimples are evident, suggesting a mixed fracture mode of ductile–brittle type. However, Fig. 5b shows that E3 fracture surface possesses a much larger number of very fine dimples isolated by sharp edges. In the case of E3A (Fig. 5c), like E3, a large number of dimples are apparent, however, the sizes of these dimples are bigger than those found in E3 due to its coarser initial grain structure. Both fracture surfaces observed in E3 and E3A samples confirm the remarkable ductile fracture behavior.

3.3. Mechanical properties at 200 °C

Fig. 6 shows the true stress versus the true strain curves for all the investigated samples tested at 200 °C and at a strain rate of 1.0×10^{-3} s^{-1}. As seen, the flow stress drop becomes less evident as ECAP proceeds and the plastic flow region expands over higher strain ranges. That is, with a decrease of the grain size, both the strain harden-ing rate and the level of the flow stress progressively decreased, while the elongation increased significantly from 140% for A samples to 300% for E3 samples. Combined observation of Figs. 6 and 7a indicates that a localized necking has taken place in sample A at an early stage of deformation, while in the case of E3 (Figs. 6 and 7b) the gradual de-velopment of necking is demonstrated through a uniform plastic flow, confirming the superplastic behavior of this sample. It is observed from Fig. 6 that E3A sample has a lower elongation than E3 and a lower flow stress than A, indicating that the peak stress is mainly texture dependent, and the elongation in contrast, is dictated by the grain size. The UFG structure of sample E3 with a grain size far below that of E3A (500 nm vs. 3.9 µm) provides an extensive amount of grain bound-aries to take part in GBS and superplastic flow. Moreover, higher fraction of grains having the favorable orientation for basal slip with higher texture intensity than that of E3A accompanied by higher prob-ability of non-basal slip systems due to grain-boundary compatibility

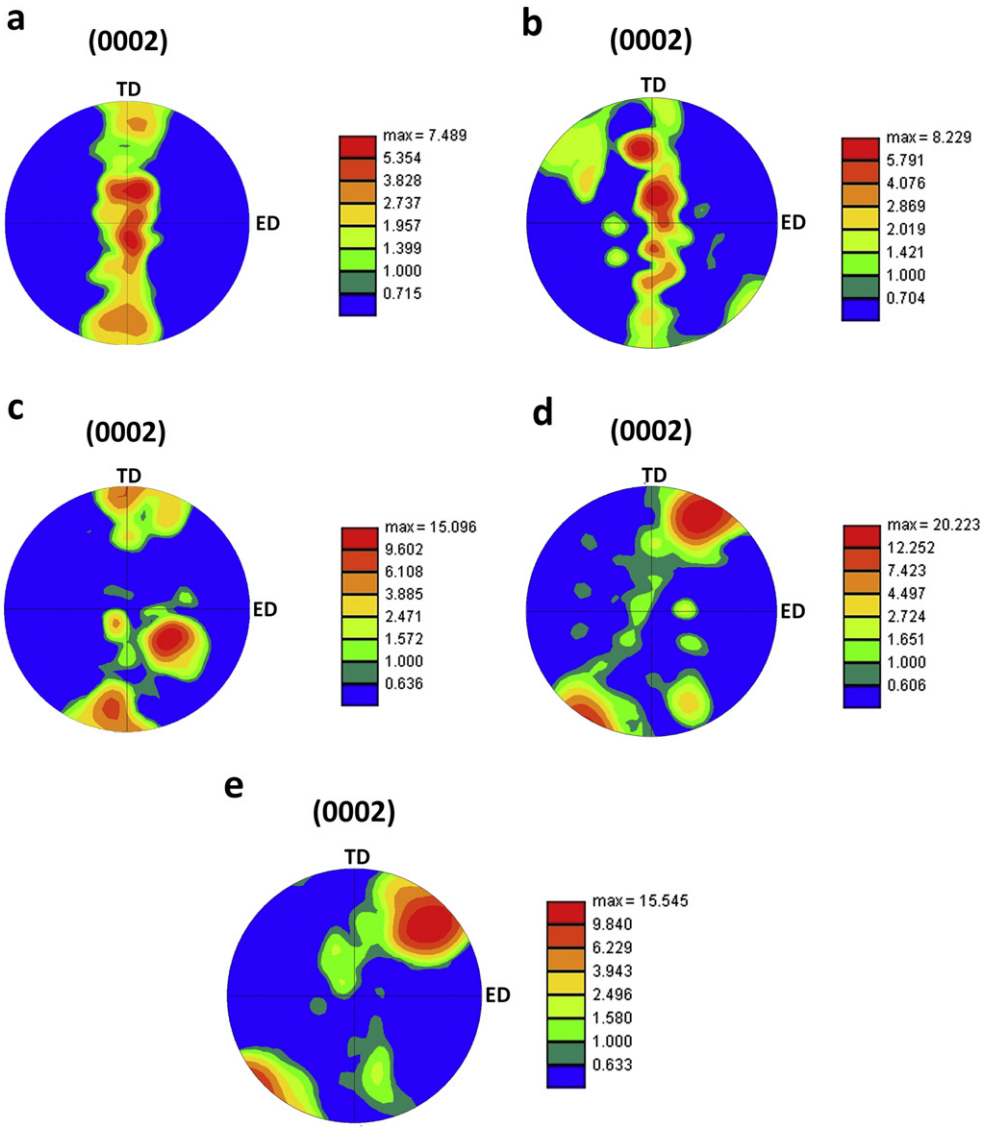

Fig. 3. (0002) pole figure showing the crystallographic texture of samples A (a), E1 (b), E2 (c), E3 (d) and E3A (e).

stress [29], caused lower yield stress in sample E3. As discussed earlier, both A and E3A exhibited similar grain size with different basal texture orientations, therefore, texture is considered to be responsible for the observed lower peak flow in E3A. Accordingly, for E3A sample the dom-inant mechanism during the deformation at 200 °C is slipping. More-over, Fig. 7c indicates the presence of localized necking and slip bands inclined to the tensile direction (ECAP direction), confirming that GBS has not actively operated during the tensile deformation and the rate controlling process has been dislocation slip.

Fig. 8 shows the SEM images of the fractured surface of A, E3 and E3A samples tested at 200 °C and a strain rate of $10^{-3}\ s^{-1}$. As seen in Fig. 8a, for sample A, compared to its fracture surface after failure at room temperature (Fig. 5a), the number of observed dimples increased considerably and they also became deeper with various size distributions arising from the initial bimodal grain structure (as seen in Fig. 1a). As known, the size of the dimples is strongly associated with the material's grain structure since it is dependent on the initiation site and the number of voids nucleated at the grain boundaries [30]. Therefore, for E3 (Fig. 8b) the fracture surface was almost entirely covered by small size plastic dimples, resulting from its equiaxed UFG structure generated by ECAP, suggesting remarkable acquired tensile elongation of 300%. Fig. 8c clearly shows the appearance of shearing planes on the fracture surface of E3A sample after deformation, emphasizing that the prevailing deformation mechanism for this sample was slipping due to the favorable basal plane orientation for dislocation slip.

Fig. 9a shows the variation of flow stress against the initial strain rate, where the flow stress for each strain rate is determined at a strain of $\varepsilon = 0.1$. As seen, the flow stress invariably increases with increasing the strain rate. It is well known that for the superplastic alloys the strain rate sensitivity exponent (m), defined as the slope in a double logarith-mic plot of flow stress versus strain rate, should be above 0.4 [31].The obtained results indicate that the m value increases with decreasing the strain rate. It is clear that for E3 the maximum m value of 0.41 was

Table 2
Schmid factor analysis results of basal slip and extension twinning systems for the investigated samples.

Mode	A	E1	E2	E3	E3A
Basal slip	0.16	0.21	0.30	0.34	0.38
Extension twining	0.42	0.39	0.34	0.32	0.31

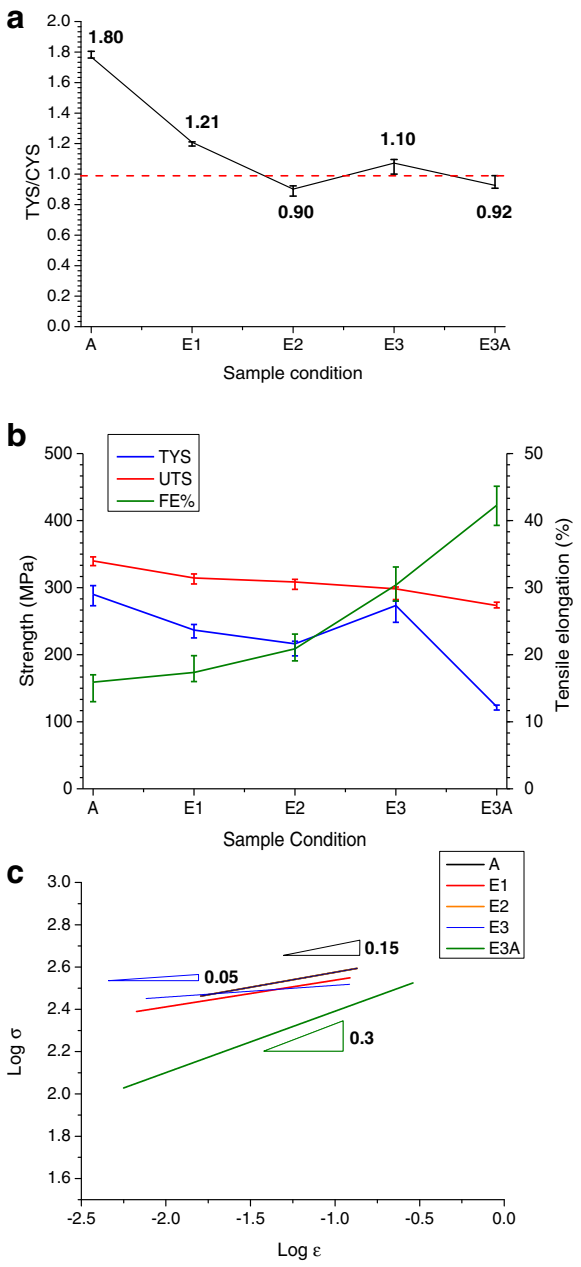

Fig. 4. (a) Yielding asymmetry, (b) tensile properties and (c) work hardening exponents calculated from the tensile curves for all the investigated samples.

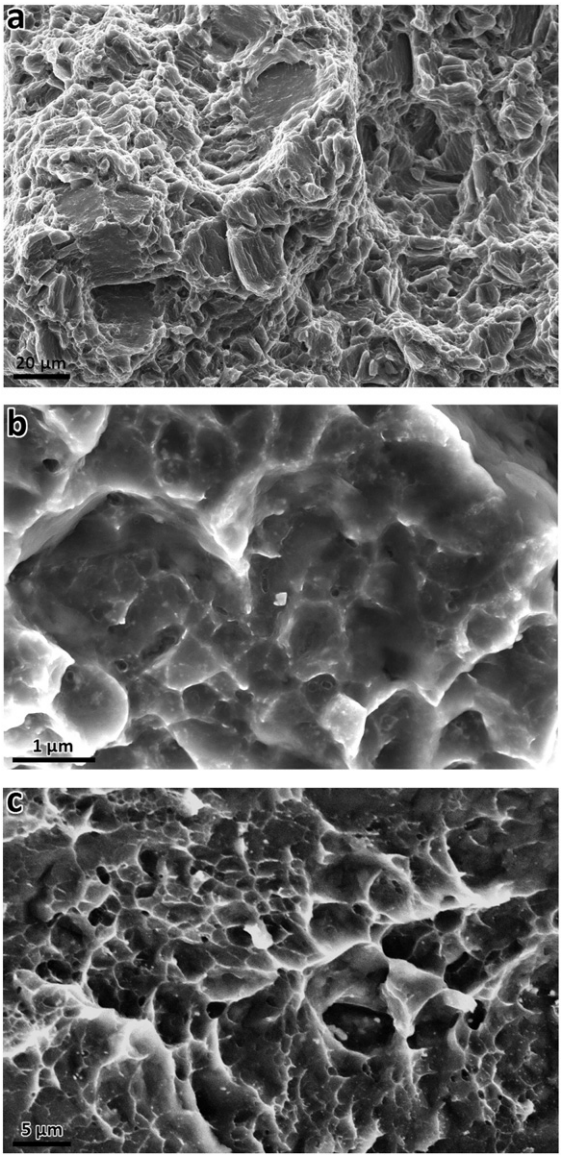

Fig. 5. The fracture surfaces of ZK60 alloy after tensile test at room temperature: (a) A, (b) E3 and (c) E3A.

achieved at the strain rate of $1.0 \times 10^{-4}\ s^{-1}$. Hence, such a high value of m confirms that slip-accommodated GBS dominates the deformation. The same increasing trend of m with strain rate was observed for A and E3A, reaching values of 0.20 and 0.24, respectively, at the strain rate of $1.0 \times 10^{-4}\ s^{-1}$. For all three samples at higher strain rates the m value was reduced so that, at a strain rate of $0.1\ s^{-1}$, it reached 0.08, 0.11 and 0.16 for A, E3 and E3A, respectively, indicating that the rate controlling deformation process at higher strain rates is dislocation slip. The measured m value for A and E3A in all tested strain rates con-firmed the occurrence of dislocation glide as the dominant rate-controlling flow mechanism. Lower placement of E3A plot compared to A at all strain rates in Fig. 9a highlights another time the favorable texture orientation for basal slip requiring a lower stress for plastic flow. It is worth mentioning that the aforementioned slip bands in Fig. 7c were observed in all the other strain rates as well.

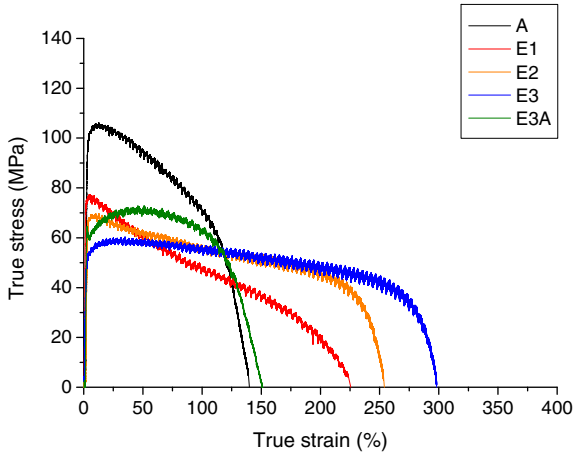

Fig. 6. True stress vs. true strain curves recorded at 200 °C and a strain rate of $1.0 \times 10^{-3}\ s^{-1}$ for the all samples.

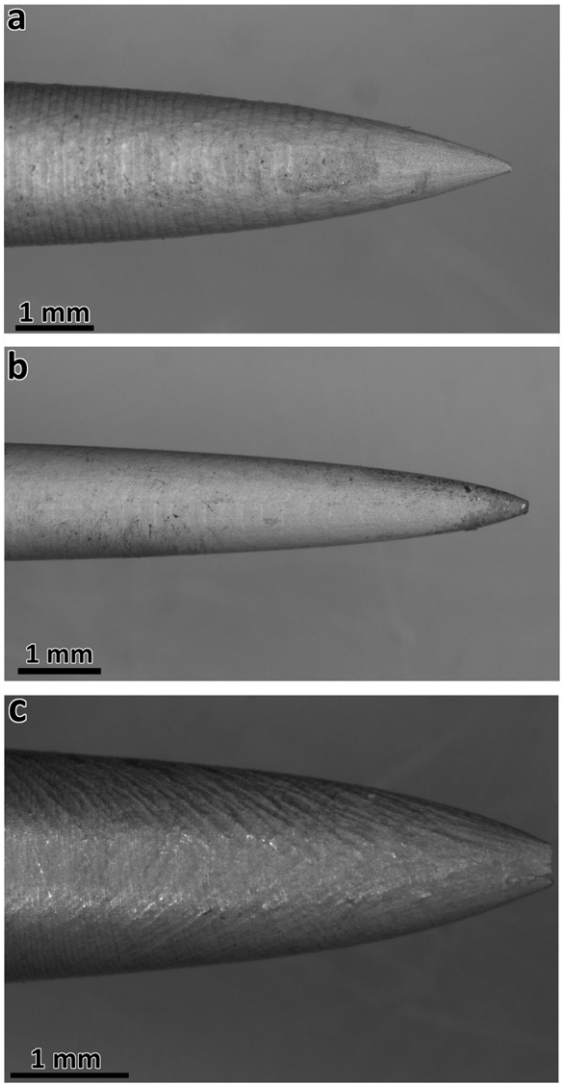

Fig. 7. General appearances of the (a) A, (b) E3 and (c) E3A samples deformed to fracture at 200 °C and at strain rate of $1.0 \times 10^{-3}\,s^{-1}$.

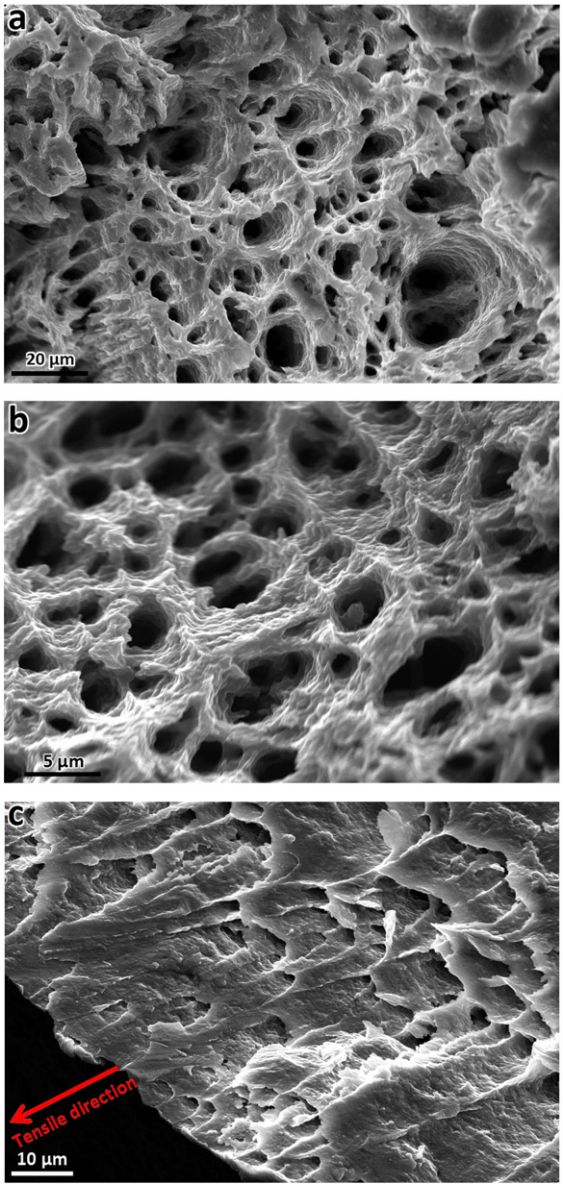

Fig. 8. SEM micrographs of fractured tensile specimens at 200 °C and a strain rate of $1.0 \times 10^{-3}\,s^{-1}$ (a) A, (b) E3 and (c) E3A.

Fig. 9b shows the elongation to failure plotted as a function of strain rate at 200 °C. The elongations of all the samples tend to increase with decreasing strain rate. However, this trend is more pronounced for sample E3 compared to A and E3A. It is apprehensible that due to the absence of GBS during the deformation of both A and E3A, their elongation to failure remains always notably below that of E3.

In the case of E3 the maximum elongation of nearly 420% was achieved at a strain rate of $1.0 \times 10^{-4}\,s^{-1}$, indicating that the alloy exhibits notable superplasticity dominated by effective contribution of GBS. In brief, although at room temperature texture dependence on elongation to failure was fully evident, this dependency became weaken and it was replaced by grain size effect so as the superplastic ductility improves as the grain size is reduced.

4. Conclusion

In summary, microstructure, texture, mechanical asymmetry and low temperature superplasticity of ZK60 Mg alloy subjected to ECAP were investigated. Significant grain refinement was obtained through ECAP giving rise to a homogenous ultrafine grain (UFG) structure with an average size of 500 nm. The initial fiber texture was gradually evolved into a new and more intense one featuring the preferential alignment of the basal planes along the ECAP shear planes with a higher Schmid factor. Microstructural and texture characterizations revealed that a combination of grain refinement and texture development led to an improvement of fracture elongation of about 100% in the UFG sample while keeping a relatively high yield and an ultimate tensile strength. Due to the high activity of basal slip, meaningful increase of the uniform elongation up to 43% and high strain hardening exponent of 0.3, comparable with those of extruded and UFG samples, was achieved in the ECAP-annealed sample. Tensile and compression tests at room temperature revealed that regardless of grain size, fracture elongation and yield asymmetry were strongly texture dependent. For the UFG sample, counterbalanced effects between grain boundary strengthening and favorable texture orientation for basal slip caused considerable improvements in both strength and fracture elongation. The stress–strain curves at 200 °C showed that the flow stress had noticeable texture dependence. However, superplastic ductility was strongly dictated by grain size, appearing only in UFG microstructure contributing to the GBS mechanism as a rate-controlling process with a

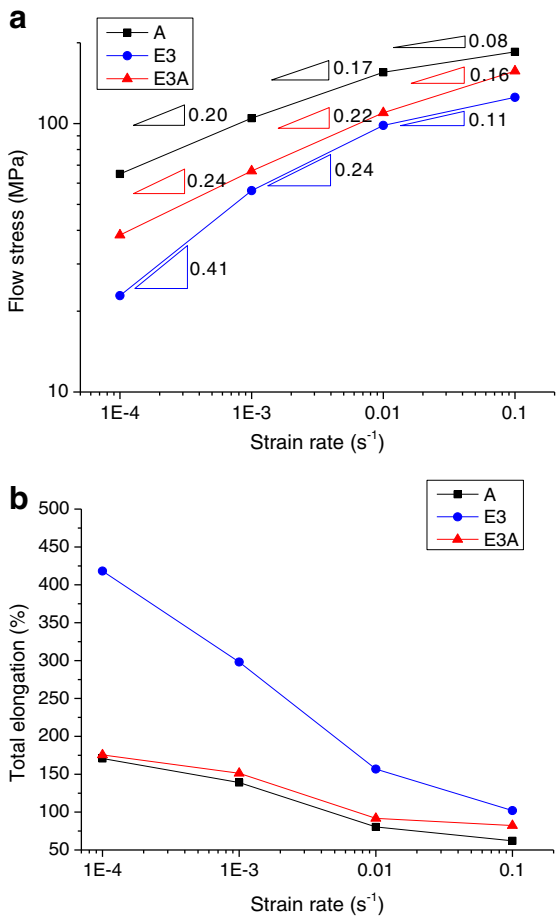

Fig. 9. The variation of (a) flow stress and (b) elongation-to-failure versus strain rate for A, E3 and E3A samples.

maximum elongation of about 420% obtained at 200 °C and at a strain rate of $1.0 \times 10^{-4}\ s^{-1}$.

References

[1] B.L. Mordike, T. Ebert, Magnesium: properties — applications — potential, Mater. Sci. Eng. A 302 (2001) 37–45, http://dx.doi.org/10.1016/S0921-5093(00)01351-4.

[2] E. Mostaed, M. Vedani, M. Hashempour, M. Bestetti, Influence of ECAP process on mechanical and corrosion properties of pure Mg and ZK60 magnesium alloy for biodegradable stent applications, Biomatter 4 (2014) e28283, http://dx.doi.org/10. 4161/biom.28283.

[3] F. Witte, N. Hort, C. Vogt, S. Cohen, K.U. Kainer, R. Willumeit, et al., Degradable biomaterials based on magnesium corrosion, Curr. Opin. Solid State Mater. Sci. 12 (2008) 63–72, http://dx.doi.org/10.1016/j.cossms.2009.04.001.

[4] M. Hakamada, T. Furuta, Y. Chino, Y. Chen, H. Kusuda, M. Mabuchi, Life cycle inven-tory study on magnesium alloy substitution in vehicles, Energy 32 (2007) 1352–1360, http://dx.doi.org/10.1016/j.energy.2006.10.020.

[5] G. Qiang, E. Mostaed, C. Zanella, Y. Zhentao, M. Vedani, Ultra-fine grained degradable magnesium for biomedical applications, Rare Met. Mater. Eng. 43 (2014) 2561–2566, http://dx.doi.org/10.1016/S1875-5372(15)60001-7.

[6] E. Mostaed, Q. Ge, M. Vedani, P.A. De Oliveira Botelho, C. Zanella, F. Deflorian, Inves-tigation on the influence of grain size on strength, ductility, and corrosion properties in Mg and Mg–Zn based alloys for biodegradable stents, Eur. Cell Mater. 26 (2013) 84.

[7] R.E. Reed-Hill, W.D. Robertson, The crystallographic characteristics of fracture in magnesium single crystals, Acta Metall. 5 (1957) 728–737, http://dx.doi.org/10. 1016/0001-6160(57)90075-5.

[8] S.G.I. Taylor, Plastic Strain in Metals, 1938.

[9] B.C. Wonsiewicz, Plasticity of Magnesium CrystalsThesis Massachusetts Institute of Technology, 1966. (http://dspace.mit.edu/handle/1721.1/27989 (accessed Decem-ber 16, 2014)).

[10] B. Srinivasarao, N.V. Dudamell, M.T. Pérez-Prado, Texture analysis of the effect of non-basal slip systems on the dynamic recrystallization of the Mg alloy AZ31, Mater. Charact. 75 (2013) 101–107, http://dx.doi.org/10.1016/j.matchar.2012.10. 002.

[11] T. Obara, H. Yoshinga, S. Morozumi, {1122} ⟨1123⟩ Slip system in magnesium, Acta Metall. 21 (1973) 845–853, http://doi.org/10.1016/0001-6160(73)90141-7.

[12] S. Yi, J. Bohlen, F. Heinemann, D. Letzig, Mechanical anisotropy and deep drawing behaviour of AZ31 and ZE10 magnesium alloy sheets, Acta Mater. 58 (2010) 592–605, http://dx.doi.org/10.1016/j.actamat.2009.09.038.

[13] S. Kleiner, P.J. Uggowitzer, Mechanical anisotropy of extruded Mg–6% Al–1% Zn alloy, Mater. Sci. Eng. A 379 (2004) 258–263, http://dx.doi.org/10.1016/j.msea.2004.02.020.

[14] S.M. Yin, C.H. Wang, Y.D. Diao, S.D. Wu, S.X. Li, Influence of grain size and texture on the yield asymmetry of Mg–3Al–1Zn alloy, J. Mater. Sci. Technol. 27 (2011) 29–34, http://dx.doi.org/10.1016/S1005-0302(11)60021-2.

[15] E. Mostaed, A. Fabrizi, D. Dellasega, F. Bonollo, M. Vedani, Microstructure, mechani-cal behavior and low temperature superplasticity of ECAP processed ZM21 Mg alloy, Alloys Compd. 638 (2015) 267–276, http://dx.doi.org/10.1016/j.jallcom.2015.03. 029.

[16] E. Mostaed, M. Hashempour, A. Fabrizi, D. Dellasega, M. Bestetti, F. Bonollo, et al., Microstructure, texture evolution, mechanical properties and corrosion behavior of ECAP processed ZK60 magnesium alloy for biodegradable applications, J. Mech. Behav. Biomed. Mater. 37 (2014) 307–322, http://dx.doi.org/10.1016/j.jmbbm.2014.05.024.

[17] J. Bohlen, P. Dobroň, J. Swiostek, D. Letzig, F. Chmelík, P. Lukáč, et al., On the influ-ence of the grain size and solute content on the AE response of magnesium alloys tested in tension and compression, Mater. Sci. Eng. A 462 (2007) 302–306, http://doi.org/10.1016/j.msea.2006.02.470.

[18] J. Jain, W.J. Poole, C.W. Sinclair, M.A. Gharghouri, Reducing the tension–compression yield asymmetry in a Mg–8Al–0.5Zn alloy via precipitation, Scr. Mater. 62 (2010) 301–304, http://dx.doi.org/10.1016/j.scriptamat.2009.11.024.

[19] T.G. Langdon, Achieving superplasticity in ultrafine-grained metals, Mech. Mater. 67 (2013) 2–8, http://dx.doi.org/10.1016/j.mechmat.2013.06.005.

[20] H.K. Lin, J.C. Huang, T.G. Langdon, Relationship between texture and low tempera-ture superplasticity in an extruded AZ31 Mg alloy processed by ECAP, Mater. Sci. Eng. A 402 (2005) 250–257, http://dx.doi.org/10.1016/j.msea.2005.04.018.

[21] K. Matsubara, Y. Miyahara, Z. Horita, T.G. Langdon, Developing superplasticity in a magnesium alloy through a combination of extrusion and ECAP, Acta Mater. 51 (2003) 3073–3084, http://dx.doi.org/10.1016/S1359-6454(03)00118-6.

[22] R.B. Figueiredo, T.G. Langdon, Strategies for achieving high strain rate superplasticity in magnesium alloys processed by equal-channel angular pressing, Scr. Mater. 61 (2009) 84–87, http://dx.doi.org/10.1016/j.scriptamat.2009.03.012.

[23] Y. Iwahashi, J. Wang, Z. Horita, M. Nemoto, T.G. Langdon, Principle of equal-channel angular pressing for the processing of ultra-fine grained materials, Scr. Mater. 35 (1996) 143–146, http://dx.doi.org/10.1016/1359-6462(96)00107-8.

[24] V.M. Segal, Equal channel angular extrusion: from macromechanics to structure for-mation, Mater. Sci. Eng. A 271 (1999) 322–333, http://dx.doi.org/10.1016/S0921-5093(99)00248-8.

[25] A. Gholinia, P.B. Prangnell, M.V. Markushev, The effect of strain path on the develop-ment of deformation structures in severely deformed aluminium alloys processed by ECAE, Acta Mater. 48 (2000) 1115–1130, http://dx.doi.org/10.1016/S1359-6454(99)00388-2.

[26] M.A. Meyers, O. Vöhringer, V.A. Lubarda, The onset of twinning in metals: a consti-tutive description, Acta Mater. 49 (2001) 4025–4039, http://dx.doi.org/10.1016/S1359-6454(01)00300-7.

[27] J.C. Tan, M.J. Tan, Dynamic continuous recrystallization characteristics in two stage deformation of Mg–3Al–1Zn alloy sheet, Mater. Sci. Eng. A 339 (2003) 124–132.

[28] J.A. del Valle, F. Carreño, O.A. Ruano, Influence of texture and grain size on work hardening and ductility in magnesium-based alloys processed by ECAP and rolling, Acta Mater. 54 (2006) 4247–4259, http://dx.doi.org/10.1016/j.actamat.2006.05.018.

[29] J. Koike, T. Kobayashi, T. Mukai, H. Watanabe, M. Suzuki, K. Maruyama, et al., The ac-tivity of non-basal slip systems and dynamic recovery at room temperature in fine-grained AZ31B magnesium alloys, Acta Mater. 51 (2003) 2055–2065, http://dx.doi. org/10.1016/S1359-6454(03)00005-3.

[30] M.-H. Cai, C.-Y. Lee, Y.-K. Lee, Effect of grain size on tensile properties of fine-grained metastable β titanium alloys fabricated by stress-induced martensite and its reverse transformations, Scr. Mater. 66 (2012) 606–609, http://dx.doi.org/10.1016/j. scriptamat.2012.01.015.

[31] O.D. Sherby, J. Wadsworth, Superplasticity—recent advances and future direc-tions, Prog. Mater. Sci. 33 (1989) 169–221, http://dx.doi.org/10.1016/0079-6425(89)90004-2.